

# <sup>1</sup> A vibecoder's guide to image analysis

<sup>2</sup> Abani Neferkara<sup>1</sup>, Asif Ali<sup>1</sup>, David Pincus<sup>1,2,3,\*</sup>

<sup>3</sup> <sup>1</sup>Department of Molecular Genetics and Cell Biology, The University of Chicago, Chicago, IL 60637, USA

<sup>4</sup> <sup>2</sup>Institute for Biophysical Dynamics, The University of Chicago, Chicago, IL 60637, USA

<sup>5</sup> <sup>3</sup>Center for Physics of Evolving Systems, The University of Chicago, Chicago, IL 60637, USA

<sup>6</sup> \*Correspondence: [pincus@uchicago.edu](mailto:pincus@uchicago.edu)

## <sup>7</sup> Abstract

<sup>8</sup> Quantitative fluorescence microscopy is central to modern cell biology, yet extracting reproducible  
<sup>9</sup> measurements from images remains a bottleneck for biologists without programming experience.  
<sup>10</sup> Here we present `cellquant`, a single script command-line pipeline that takes arbitrary fluores-  
<sup>11</sup> cence images of any cell type and performs cell segmentation, colocalization analysis, puncta  
<sup>12</sup> quantification, and/or spatial proximity measurements. Combined with a comprehensive tutorial,  
<sup>13</sup> `cellquant` is configured entirely through human-readable arguments rather than code editing, with  
<sup>14</sup> AI chatbots bridging the gap between biological expertise and computational analysis. We validate  
<sup>15</sup> the pipeline on two biological systems: arsenite-induced stress granule formation in human tissue  
<sup>16</sup> culture cells and temperature-dependent nucleolar reorganization in budding yeast. The pipeline  
<sup>17</sup> produces publication-ready quantification with statistically rigorous replicate analysis and QC  
<sup>18</sup> overlays for visual validation. All code, documentation, and example datasets are freely available.

## <sup>19</sup> Introduction

<sup>20</sup> Fluorescence microscopy provides the visual evidence underlying much of modern cell biology.  
<sup>21</sup> Advances in segmentation algorithms, particularly deep learning approaches such as Cellpose  
<sup>22</sup> [[Stringer et al., 2021](#), [Pachitariu and Stringer, 2022](#)], have largely solved the technical challenge  
<sup>23</sup> of identifying individual cells in microscopy images. Similarly, well-established algorithms exist  
<sup>24</sup> for detecting sub-cellular structures, computing colocalization metrics, and measuring spatial  
<sup>25</sup> relationships between cellular compartments.

<sup>26</sup> Despite the availability of these algorithms, a persistent gap remains between the existence  
<sup>27</sup> of computational tools and their routine use by experimental biologists. This gap is primarily  
<sup>28</sup> architectural rather than technical. Individual algorithms must be assembled into coherent pipelines  
<sup>29</sup> that handle the full workflow from raw image to statistical summary. This assembly step frequently  
<sup>30</sup> requires bespoke processing requiring programming, which creates a barrier that excludes a  
<sup>31</sup> large fraction of the experimental biology community from performing their own quantitative  
<sup>32</sup> analysis. Several excellent tools address this barrier. CellProfiler [[Stirling et al., 2021](#)] provides a  
<sup>33</sup> graphical pipeline builder; Fiji/ImageJ [[Schindelin et al., 2012](#)] offers macro-based automation;

34 napari [Sofroniew et al., 2022] provides interactive visualization with plugin extensibility. However,  
35 each requires the user to learn a software-specific workflow, and configuring these tools for novel  
36 biological contexts still often demands computational expertise or support from a bioinformatician.

37 The emergence of large language model (LLM)-based coding assistants (e.g., Claude, Chat-  
38 GPT, GitHub Copilot) introduces a fundamentally different paradigm. Rather than learning to  
39 program, a biologist can describe their analysis in natural language and have an AI assistant  
40 generate or configure the necessary code. This approach, colloquially termed “vibecoding”, is  
41 particularly well-suited to image analysis, where the domain expertise of the biologist (recognizing  
42 correct segmentation, identifying biologically meaningful structures, evaluating whether results are  
43 reasonable) is precisely what is needed to supervise and validate automated pipelines (Figure 1A).

44 Among the most demanding areas of modern cell biology for image analysis is the study  
45 of biomolecular condensates: membraneless compartments assembled through multivalent in-  
46 teractions among proteins and nucleic acids that form, dissolve, and reorganize in response to  
47 environmental conditions [Banani et al., 2017]. Condensate dynamics are regulated by diverse  
48 mechanisms including molecular chaperones [Bard and Drummond, 2024] and post-translational  
49 modifications such as urmylation [Cairo et al., 2024]. Unlike stable organelles with well-defined  
50 morphologies, condensates vary in number, size, and intensity across conditions, require segmenta-  
51 tion at multiple spatial scales, and often must be interpreted through spatial relationships between  
52 structures rather than simple counts. Stress granules, cytoplasmic ribonucleoprotein assemblies  
53 that form when translation initiation is inhibited by diverse stresses [Protter and Parker, 2016],  
54 exemplify these challenges. Recent work has revealed that transcriptome-wide mRNP condensation  
55 is a pervasive response to stress that can occur independently of visible stress granule formation  
56 [Glauninger et al., 2025]. Stress granule assembly is driven by the RNA-binding protein G3BP1,  
57 which functions as a molecular switch triggering liquid-liquid phase separation in response to  
58 increased cytoplasmic mRNA concentrations [Yang et al., 2020, Guillén-Boixet et al., 2020] and rein-  
59 forces the integrated stress response translation program [Smith and Bartel, 2026]. Stress granules  
60 are increasingly recognized as nodes in broader condensate networks that coordinate the cellular  
61 stress response, including the heat shock response [Pincus, 2020, Dea and Pincus, 2024] and the  
62 unfolded protein response [Pincus, 2024].

63 The nucleolus, the site of ribosome biogenesis [Shore et al., 2021], is itself a multilayered  
64 condensate that serves as an exquisitely sensitive gauge of cellular stress [Boulon et al., 2010,  
65 Lafontaine et al., 2021]. Heat stress causes dramatic nucleolar compaction and reorganization in  
66 yeast, reflecting shutdown of rRNA synthesis and redistribution of ribosome biogenesis factors  
67 [Matos-Perdomo and Machín, 2019], a process driven in part by the self-interaction of intrinsically  
68 disordered regions within small nucleolar RNPs [Dominique et al., 2024]. During heat shock, orphan  
69 ribosomal proteins that can no longer be incorporated into ribosomes accumulate as reversible  
70 peri-nucleolar condensates maintained by the Hsp70 co-chaperone Sis1/DnaJB6, establishing a  
71 direct mechanistic link between nucleolar biology and the proteostasis network [Ali et al., 2023,  
72 2024]. Additional connections between ribosome assembly and protein quality control have

73 emerged through the finding that K29-linked polyubiquitin chains can disrupt ribosome biogenesis  
74 and direct orphan ribosomal proteins to nuclear quality control compartments [Garadi Suresh  
75 et al., 2024], highlighting the broader importance of spatial protein quality control in cellular  
76 homeostasis [Kaganovich et al., 2008, Sontag et al., 2017, 2023]. Quantifying stress granule number  
77 and composition, nucleolar morphology, protein colocalization, and spatial proximity between  
78 condensates and organelles requires a flexible multi-parameter image analysis pipeline.

79 Here we present `cellquant`, a single Python script that implements a configurable image  
80 analysis pipeline for multi-channel fluorescence microscopy. The design philosophy prioritizes  
81 accessibility: all parameters are set through command-line arguments, cell-type presets encode  
82 organism-specific defaults, and visual QC overlays enable validation by users without program-  
83 ming knowledge. We pair the pipeline with a comprehensive tutorial that walks users through  
84 installation, execution, and interpretation with explicit commands and guidance using AI assistants  
85 to customize the analysis.

86 We validate the pipeline on two complementary biological systems that illustrate its versatility:  
87 arsenite-induced stress granule formation from three-channel images (DAPI, G3BP1, PABPC1)  
88 in human U2OS cells with biological replicates enabling superplot-style statistical analysis; and  
89 temperature-dependent protein condensation and nucleolar reorganization in budding yeast, using  
90 three-channel images (Tif6, Nsr1, Sis1) across a 25–40°C temperature series with colocalization,  
91 nucleolar proximity, and morphometric quantification. Together, these examples demonstrate that  
92 a biologist who cannot write a line of code can perform publication quality quantitative image  
93 analysis.

## 94 Results

### 95 A single-script pipeline for multi-channel fluorescence image analysis

96 The `cellquant.py` script is a 1,941-line Python script that implements a complete image analysis  
97 pipeline from segmentation through statistical visualization (Figure 1B). The pipeline accepts  
98 multi-channel TIFF maximum intensity projections (MIPs) and processes them through a modular  
99 series of steps: cell segmentation using Cellpose [Pachitariu and Stringer, 2022], optional nuclear  
100 segmentation, puncta detection via Laplacian-of-Gaussian filtering, per-cell metric computation,  
101 and statistical visualization.

102 The key design decision is that all configuration occurs through command-line arguments  
103 rather than code modification. Channel identity and role are specified using a human-readable  
104 syntax, where each channel is assigned a position, a name, and a functional role. Cell-type  
105 presets (`--cell-type mammalian`, `--cell-type yeast`, `--cell-type bacteria`) provide organism-  
106 appropriate defaults for segmentation parameters, including Cellpose model selection, cell diameter,  
107 downsampling factor, and area filtering bounds. All preset values can be overridden by explicit  
108 command-line arguments, providing flexibility without requiring the user to understand the full  
109 parameter space.

110 **Quantification of arsenite induced stress granules in human cells**

111 To validate the pipeline on a well-characterized biological system, we analyzed three-channel  
112 fluorescence images of U2OS cells stably expressing the stress granule nucleator G3BP1-GFP [Yang  
113 et al., 2020] and the poly(A)-binding protein PABPC1-mCherry, both canonical stress granule  
114 markers, stained with DAPI and treated with or without 500  $\mu$ M sodium arsenite (Fig. 2A). Arsenite  
115 triggers eIF2 $\alpha$  phosphorylation through the kinase HRI, leading to global translational arrest and  
116 the condensation of stalled mRNPs into G3BP1-positive stress granules that recruit additional  
117 RNA-binding proteins including PABPC1 [Kedersha et al., 2016, Protter and Parker, 2016]. Images  
118 were acquired as maximum intensity projections from z-stacks, with 4–5 biological replicates per  
119 condition.

120 Cell segmentation using Cellpose with 3 $\times$  downsampling (which acts as spatial regularization  
121 for mammalian cell images) produced clean cell and nuclear boundaries validated by QC overlays  
122 (Fig. 2A, segmentation panels). Puncta were detected independently in the G3BP1 and PABPC1  
123 channels using Laplacian-of-Gaussian filtering within the cytoplasmic compartment (cell mask  
124 minus nuclear mask).

125 Per-cell quantification confirmed the expected arsenite-induced stress granule phenotype:  
126 increased puncta number, increased puncta area, and increased fraction of signal in condensed  
127 form in both G3BP1 and PABPC1 channels (Fig. 2B). Statistical analysis followed a superplot  
128 framework [Lord et al., 2020], in which per-cell measurements are displayed as individual data  
129 points but statistical tests (Wilcoxon rank-sum) operate on replicate-level medians. This approach  
130 produces honest *p*-values that reflect the true number of independent observations (biological  
131 replicates), rather than inflated significance from pseudoreplication.

132 Notably, with 4–5 biological replicates, only the PABPC1 fraction condensed metric reached  
133 conventional significance (*p* = 0.01), while other metrics showed strong trends (*p* = 0.08–0.14)  
134 despite visually obvious effects at the single-cell level (Fig. 2B). This illustrates a key teaching point:  
135 correct statistical treatment of biological replicates often yields modest *p*-values, and this reflects  
136 the reality of experimental power rather than a failure of the analysis.

137 **Multi-parameter analysis of temperature-dependent responses in yeast**

138 To demonstrate the pipeline's ability to generalize across organisms and analysis types, we analyzed  
139 three-channel fluorescence images of budding yeast expressing Tif6-Halo (a late ribosome biogene-  
140 sis factor involved in 60S subunit maturation and export, labeled with Janelia Fluor 646 HaloTag  
141 ligand), Nsr1-mScarlet-I (a dense fibrillar component nucleolar marker and the yeast homolog  
142 of mammalian nucleolin), and Sis1-mVenus (an Hsp40 co-chaperone of Hsp70 that relocates to  
143 peri-nucleolar condensates during heat shock to maintain orphan ribosomal proteins in a soluble,  
144 reversible state; Ali et al. 2023) at five temperatures from 25°C to 40°C (Fig. 3A).

145 For yeast segmentation, the pipeline used Cellpose with no downsampling (appropriate given  
146 the ~5  $\mu$ m cell diameter) and composite-channel input (sum of all channels) since no dedicated

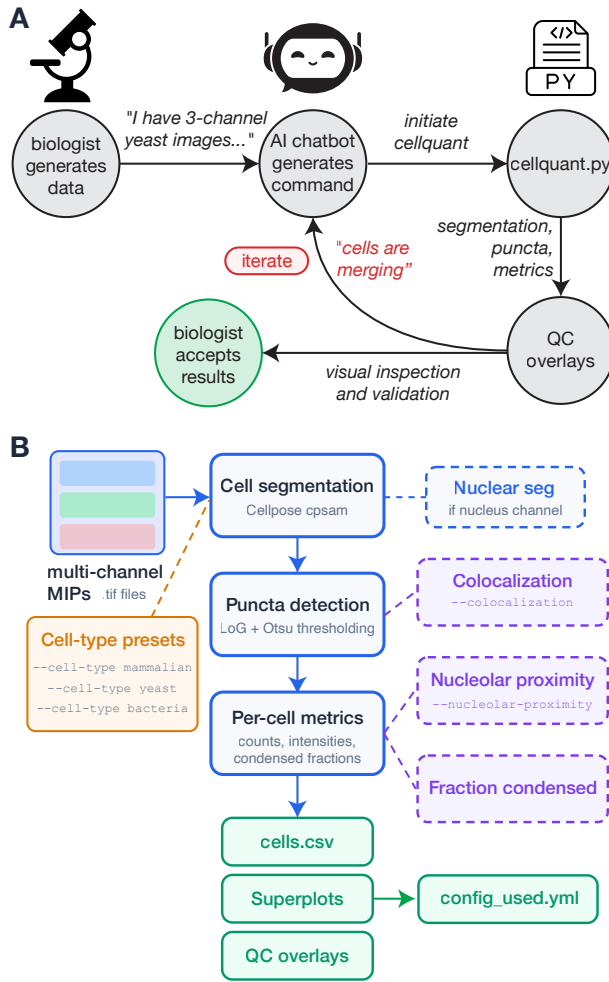


**Figure 1: Vibecoder workflow and cellquant pipeline.** **(A)** The vibecoder workflow. The biologist describes their analysis needs to an AI assistant, which generates the appropriate command-line invocation of `cellquant.py`. The pipeline produces segmentation, puncta detection, per-cell metrics, and QC overlays that the biologist evaluates visually. If results are incorrect, the biologist describes the problem to the AI, which adjusts parameters. This loop continues until the output matches the biologist's expectations. **(B)** Schematic of the pipeline architecture. Multi-channel fluorescence MIPs are processed through cell segmentation (Cellpose cpsam), optional nuclear segmentation, puncta detection (Laplacian-of-Gaussian with Otsu thresholding), and per-cell metric computation. Cell-type presets provide organism-specific defaults. Modular analysis modules (colocalization, nucleolar proximity, fraction condensed) are activated by command-line flags. Outputs include per-cell metrics (`cells.csv`), superplots, QC overlays, and a record of all parameters (`config_used.yml`).

<sup>147</sup> nuclear stain was available. Area filtering (200–5,000 pixels) removed debris and merged cell  
<sup>148</sup> clusters. The nucleolus channel role was used for Nsr1, directing the pipeline to generate per-cell  
<sup>149</sup> nucleolar masks via Otsu thresholding rather than using Nsr1 for nuclear segmentation.

<sup>150</sup> **Nucleolar morphology, colocalization, and Sis1 nucleolar proximity across temperatures**

<sup>151</sup> Nucleolar morphometrics (area, solidity, circularity, eccentricity) were computed from the Nsr1-  
<sup>152</sup> derived nucleolar mask for each cell (Fig. 3B). Nucleolar circularity increased monotonically with  
<sup>153</sup> temperature, reflecting the well-characterized transition from crescent-shaped nucleoli in actively  
<sup>154</sup> growing cells to rounded, compact nucleoli in stressed or growth-arrested cells [Matos-Perdomo  
<sup>155</sup> and Machín, 2019]. Nucleolar area showed a corresponding increase at elevated temperatures,  
<sup>156</sup> consistent with nucleolar reorganization under stress.

<sup>157</sup> Pairwise colocalization (Pearson’s correlation coefficient with Costes automatic thresholding;  
<sup>158</sup> Costes et al. 2004) was computed for all three channel pairs across the temperature series (Fig. 3B).  
<sup>159</sup> Nsr1-Tif6 colocalization was high at permissive temperatures (both proteins are nucleolar) but  
<sup>160</sup> decreased at 40°C, consistent with Tif6 redistribution during ribosome biogenesis shutdown under  
<sup>161</sup> severe heat stress.

<sup>162</sup> The pipeline computed the distance from each Sis1 spot centroid to the nearest nucleolar  
<sup>163</sup> boundary (defined by the Nsr1 mask), enabling quantification of whether chaperone condensates  
<sup>164</sup> form preferentially near the nucleolus (Fig. 3B). This measurement is motivated by the finding  
<sup>165</sup> that Sis1-containing condensates harboring orphan ribosomal proteins accumulate at the nucleolar  
<sup>166</sup> periphery during heat shock [Ali et al., 2023], raising the question of how condensate spatial  
<sup>167</sup> organization varies across the physiological temperature range. QC overlays color-code puncta as  
<sup>168</sup> proximal (red,  $\leq 5$  pixels from nucleolus) or distal (blue), enabling visual validation of the spatial  
<sup>169</sup> measurements.

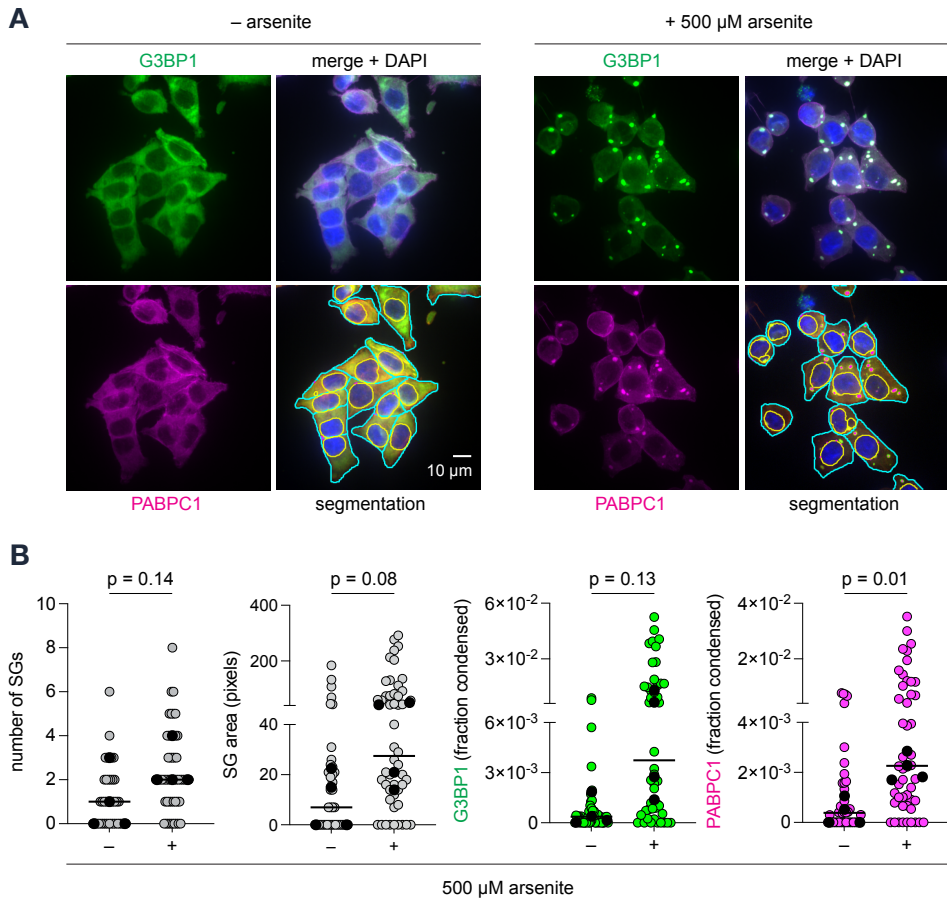


**Figure 2: Quantification of arsenite-induced stress granules in mammalian cells.** (A) Representative fluorescence images of U2OS cells  $\pm$  500  $\mu$ M arsenite. Top: individual channels (G3BP1, green; PABPC1, magenta) and merge with DAPI (blue). Bottom: segmentation overlays showing cell boundaries (cyan), nuclear boundaries (yellow), and detected puncta. Scale bar, 10  $\mu$ m. (B) Quantification of stress granule metrics. From left to right: number of stress granules per cell, stress granule area (pixels), fraction of G3BP1 signal in condensed form, fraction of PABPC1 signal in condensed form. Black filled circles represent replicate medians; gray / colored circles represent individual cells. Lines indicate overall medians.  $P$ -values from Wilcoxon rank-sum test on replicate medians.

170 **The vibecoder workflow in practice**

171 The pipeline was developed iteratively using the AI coding assistant Claude (Anthropic) through a  
172 process that exemplifies the vibecoder workflow. The initial mammalian cell pipeline was built  
173 in a single session by describing the desired analysis in natural language and refining based  
174 on QC overlay evaluation. Extension to yeast required specifying new requirements (nucleolar  
175 segmentation, colocalization, spatial proximity) that were translated into a formal specification  
176 document, implemented by the AI, and validated through the same visual QC loop.

177 Several episodes in the development process illustrate both the power and the current limita-  
178 tions of AI-assisted scientific programming. When we upgraded to Cellpose 4, model loading failed  
179 because the API changed how it distinguishes built-in from custom model paths, but the AI identi-  
180 fied and resolved this across three iterations of error messages and proposed fixes. Separately, the  
181 Cellpose Transformer model (cpsam) turned out not to support certain Apple processors, requiring  
182 an automatic fallback that was identified empirically and resolved. Perhaps most instructively,  $3 \times$   
183 downsampling before Cellpose segmentation, initially implemented for speed, produced better  
184 segmentation for mammalian cells by suppressing noise but had to be disabled for yeast cells where  
185 the smaller cell size made downsampling destructive.

186 These are not bugs to be hidden. They are the kinds of issues that arise routinely in computa-  
187 tional biology, and a vibecoder must be equipped to navigate them by describing the symptoms to  
188 an AI assistant and evaluating the proposed fixes.

189 **Installation, tutorial, and documentation**

190 To access the pipeline, `cellquant` is distributed as a single Python script alongside an environ-  
191 ment specification (`environment.yml`) and a suite of documentation designed to make the entire  
192 workflow navigable without prior programming experience. Installation requires download-  
193 ing the repository and creating the environment with a single command; on a typical laptop this  
194 takes 10–15 minutes, with the Cellpose models constituting the majority of the download. De-  
195 tailed platform-specific instructions for macOS, Windows, and Linux are provided in `INSTALL.md`,  
196 including explicit commands for users who have never opened a terminal.

197 The tutorial walks the user from first launch through a complete analysis of the included  
198 example datasets, with expected outputs at each step so the user can verify that the pipeline is  
199 working correctly before applying it to their own data. Rather than teaching Python, the tutorial  
200 teaches a different skill: how to describe an analysis problem to an AI assistant in enough detail to  
201 get a working `cellquant` command. This includes guidance on how to specify channel roles, how  
202 to interpret QC overlays, and how to communicate common failure modes (“cells are merging,”  
203 “puncta are being detected in the nucleus,” “the nucleolar mask is too aggressive”) in language that  
204 an AI assistant can translate into parameter adjustments.

205 A complete command line interface (CLI) reference (`CLI_REFERENCE.md`) documents every  
206 argument with its default value, valid range, and interaction with cell-type presets. This reference

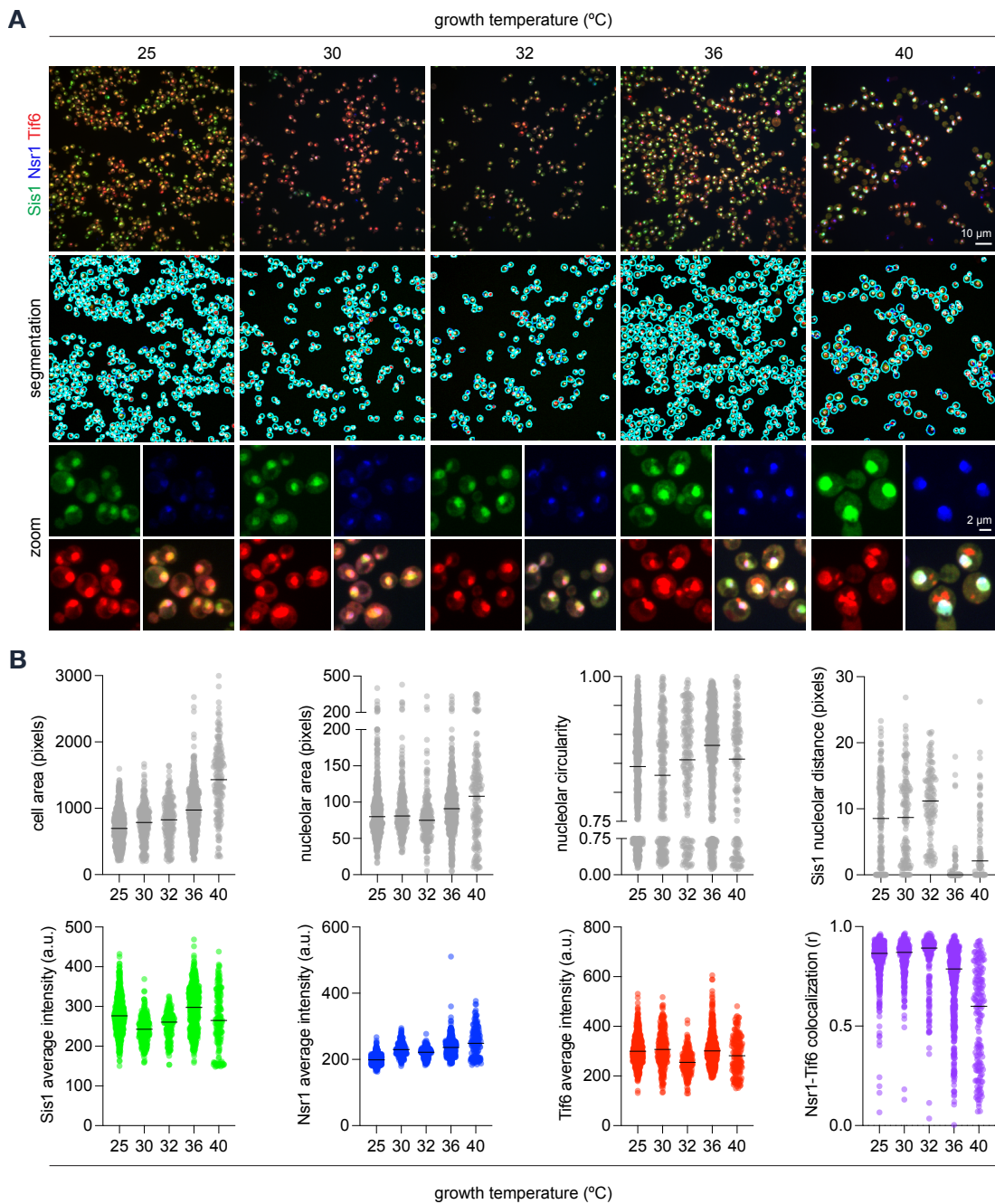


**Figure 3: Multi-parameter analysis of temperature-dependent responses in budding yeast.** **(A)** Top: representative three-channel fluorescence images across the temperature series (25–40°C). Sis1-mVenus (green), Nsr1-mScarlet-I (blue), Tif6-Halo/JF646 (red). Middle: segmentation overlays with cell boundaries (cyan), nucleolar boundaries (white). Bottom: zoomed panels showing individual cells. Scale bars, 10 μm (overview) and 2 μm (zoom). **(B)** Quantification of cellular parameters across the temperature series. Top row: cell area, nucleolar area, nucleolar circularity, Sis1 nucleolar proximity (mean distance from Sis1 puncta to nearest nucleolar boundary). Bottom row: Sis1 mean intensity, Nsr1 mean intensity, Tif6 mean intensity, Nsr1-Tif6 colocalization (Pearson's  $R$ ). Individual cells shown as scatter points; lines indicate condition medians.

207 is structured to be readable by both humans and AI chatbots, so that a user can paste it into a  
208 conversation and ask the AI to find the relevant parameter. The repository also includes a quickstart  
209 guide with a single copy-paste command that runs the pipeline on the included data, producing  
210 results in under a minute, providing immediate feedback that the installation succeeded and a  
211 concrete starting point for customization.

212 **Discussion**

213 The approach presented here rests on a simple observation: the bottleneck in biological image  
214 analysis is architectural not algorithmic. Validated algorithms exist for virtually every step of a  
215 standard analysis pipeline. What prevents most bench biologists from using them is the program-  
216 ming required to connect these algorithms into a coherent workflow. AI coding assistants eliminate  
217 this barrier by translating natural language descriptions into functional code.

218 This is not a claim that AI can replace computational biologists. Complex analysis pipelines,  
219 novel algorithms, and performance-critical applications will continue to require programming  
220 expertise. Rather, we argue that for standard analyses including cell segmentation, colocalization,  
221 puncta counting, and spatial measurements the combination of a well-designed command line tool  
222 and an AI assistant is sufficient for a biologist to produce rigorous, reproducible quantification.

223 Several design choices in `cellquant` prioritize accessibility. Distributing the pipeline as a single  
224 Python script eliminates installation complexity. The user downloads one file. There is no pip  
225 install, no import resolution, and no version conflict between subpackages. Dependencies are  
226 managed through environment specification. A CLI is less intuitive than a graphical user interface  
227 for first-time users but is fundamentally more reproducible: the exact command used to generate  
228 results can be recorded, shared, and re-executed. Critically, CLIs are legible to AI assistants,  
229 enabling the vibecoder workflow in which the user describes their needs and the AI generates the  
230 appropriate command.

231 The pipeline enforces replicate-level statistical testing, which can produce unsatisfying  $p$ -values  
232 when the number of biological replicates is small. We view this as a feature rather than a limitation.  
233 The visual display of per-cell data allows the reader to evaluate effect sizes directly, while the  
234 replicate-level test provides an honest assessment of statistical evidence. Inflating significance  
235 through pseudo-replication is a well-documented problem in biological image analysis [Lord et al.,  
236 2020, Lazić, 2018], and tools should not facilitate it.

237 The modular design of the CLI supports straightforward extension to additional analysis  
238 types. Planned additions include 3D segmentation for confocal stacks, time-series analysis for  
239 live imaging, machine learning-based phenotype classification, and integration with plate-based  
240 screening workflows. The cell-type preset system can be extended to additional organisms (e.g.,  
241 *Drosophila*, *C. elegans*, plant cells) as validated parameter sets are established.

242 More broadly, we envision `cellquant` as a template for AI-accessible scientific software. The  
243 principles demonstrated here of human-readable configuration, visual validation, honest statistics,  
244 and comprehensive documentation are not specific to image analysis. Any computational workflow

245 that can be parameterized through a CLI can be made accessible to domain experts through the  
246 same vibecoder approach.

247 **Limitations of the study**

248 The current pipeline is limited to maximum intensity projections and does not handle 3D segmen-  
249 tation or time-lapse analysis. The puncta detection algorithm (Laplacian-of-Gaussian) assumes  
250 approximately circular puncta and may not perform well on elongated or irregularly shaped  
251 structures. The colocalization analysis uses global Costes thresholding, which may not be optimal  
252 for highly heterogeneous cell populations.

253 The vibecoder workflow itself has limitations. The user must be able to evaluate QC overlays  
254 and recognize when segmentation is incorrect. This requires familiarity with the biological system  
255 being imaged. Additionally, the user's ability to communicate effectively with an AI assistant  
256 depends on being able to describe problems in sufficient detail—a skill that develops with practice.

257 **Materials and Methods**

258 **Cell culture and treatment**

259 **Mammalian cells.** U2OS cells stably expressing G3BP1-GFP and PABPC1-mCherry were cultured  
260 in DMEM supplemented with 10% FBS at 37°C with 5% CO<sub>2</sub>. For stress granule induction, cells  
261 were treated with 500 µM sodium arsenite for 45 minutes or left untreated (vehicle control). Cells  
262 were fixed with 4% paraformaldehyde and 4% sucrose, quenched with 125 mM glycine, and stained  
263 with DAPI as described [Ali et al., 2023]. G3BP1-GFP and PABPC1-mCherry signals are from the  
264 stably expressed fluorescent fusion proteins.

265 **Yeast cells.** Budding yeast (*Saccharomyces cerevisiae*, W303 background) expressing endogenously  
266 tagged Sis1-mVenus, Tif6-HaloTag, and Nsr1-mScarlet-I (strain construction as described in Ali  
267 et al. 2023) were grown to mid-log phase at 30°C in synthetic complete medium. Tif6-HaloTag  
268 was labeled with Janelia Fluor 646 HaloTag ligand (JF646, 1 µM) as described [Ali et al., 2023]. For  
269 the temperature series, aliquots were shifted to 25, 30, 32, 36, or 40°C for 6 hours starting from a  
270 pre-grown log-phase culture at 30°C. Cells were fixed in 1% paraformaldehyde as described [Garde  
271 et al., 2024].

272 **Image acquisition**

273 All images were acquired on a Nikon SoRa spinning disk confocal microscope (63× objective) at  
274 the University of Chicago Integrated Light Microscopy Core (RRID: SCR\_019197). Exposure time  
275 was 100 ms per channel for all acquisitions. Images were collected as z-stacks and converted to  
276 maximum intensity projections (MIPs) prior to analysis. For U2OS cells, z-stacks consisted of 10

277 slices at 0.25  $\mu\text{m}$  step size. For yeast, z-stacks consisted of 71 slices at 0.1  $\mu\text{m}$  step size. Pixel size  
278 was 0.094  $\mu\text{m}/\text{pixel}$  for both datasets ( $1192 \times 1200$  pixels =  $112.5 \times 113.3 \mu\text{m}$  field of view).

279 **Image analysis pipeline**

280 All image analysis was performed using `cellquant.py` (version 1.0, available at <https://github.com/davidpincus/cellquant>). The pipeline was run locally on a MacBook Pro (Apple M-series  
281 processor) using CPU-mode Cellpose due to MPS GPU incompatibility with the cpsam Transformer  
282 model.

284 **Mammalian cell analysis.** Images were processed with the following command:

```
285
286 python cellquant.py /path/to/images/ \
287     "1:DAPI:nucleus" "2:G3BP1:quantify" "3:PABPC1:quantify" \
288     --cell-type mammalian \
289     --out /path/to/output/ \
290     --filename-pattern "MAX_{condition}_rep{replicate}"
```

292 Key parameters (from the mammalian preset): Cellpose cpsam model,  $3\times$  downsampling, cell  
293 diameter 120 pixels, puncta detection in the cytoplasmic compartment (cell minus nucleus).

294 **Yeast cell analysis.** Images were processed with the following command:

```
295
296 python cellquant.py /path/to/images/ \
297     "1:Tif6:quantify" "2:Nsr1:nucleolus" "3:Sis1:quantify" \
298     --cell-type yeast \
299     --out /path/to/output/ \
300     --colocalization \
301     --nucleolar-proximity Nsr1 \
302     --puncta-channels Sis1 Tif6 \
303     --trend \
304     --filename-pattern "MAX_{condition}_rep{replicate}"
```

306 Key parameters (from the yeast preset): Cellpose cpsam model, no downsampling, cell diameter  
307 40 pixels, composite-channel segmentation input, cell area filtering (200–5,000 pixels), whole-cell  
308 puncta detection.

309 **Statistical analysis**

310 Per-cell measurements were summarized at the replicate (image) level using medians. For two-  
311 condition comparisons, Wilcoxon rank-sum tests were performed on replicate-level medians. For  
312 multi-condition temperature series (single replicate per condition), data are presented descriptively  
313 without statistical testing. Superplots display per-cell data as jittered scatter plots with replicate  
314 medians marked as diamonds.

315 **Software and reproducibility**

316 The complete analysis environment is specified in `environment.yml` and includes Python 3.11+,  
317 Cellpose 4.x, scikit-image 0.26, numpy, pandas, matplotlib, scipy, and PyYAML. All code, example  
318 data, and expected outputs are available at <https://github.com/davidpincus/cellquant>. Full  
319 datasets are deposited at Zenodo (DOI: 10.5281/zenodo.18760422).

320 **Acknowledgments**

321 We thank Madeline Herwig and members of the Bardwell and Jakob labs for beta testing `cellquant`  
322 and providing valuable feedback. We acknowledge the University of Chicago Integrated Light  
323 Microscopy Core (RRID: SCR\_019197) for microscopy support. This work was supported by NIH  
324 grants R01 GM138689 and RM1 GM153533 and NSF QLCI QuBBE grant OMA-2121044 to D.P.

325 **References**

- 326 Carsen Stringer, Tim Wang, Michalis Michaelos, and Marius Pachitariu. Cellpose: a generalist  
327 algorithm for cellular segmentation. *Nature Methods*, 18(1):100–106, 2021. doi: 10.1038/s41592-  
328 020-01018-x.
- 329 Marius Pachitariu and Carsen Stringer. Cellpose 2.0: how to train your own model. *Nature Methods*,  
330 19(12):1634–1641, 2022. doi: 10.1038/s41592-022-01663-4.
- 331 David R Stirling, Madison J Swain-Bowden, Alice M Lucas, Anne E Carpenter, Beth A Cimini, and  
332 Allen Goodman. CellProfiler 4: improvements in speed, utility and usability. *BMC Bioinformatics*,  
333 22(1):433, 2021. doi: 10.1186/s12859-021-04344-9.
- 334 Johannes Schindelin, Ignacio Arganda-Carreras, Erwin Frise, Verena Kaynig, Mark Longair, Tobias  
335 Pietzsch, Stephan Preibisch, Curtis Rueden, Stephan Saalfeld, Benjamin Schmid, Jean-Yves  
336 Tinevez, Daniel James White, Volker Hartenstein, Kevin Eliceiri, Pavel Tomancak, and Albert  
337 Cardona. Fiji: an open-source platform for biological-image analysis. *Nature Methods*, 9(7):  
338 676–682, 2012. doi: 10.1038/nmeth.2019.
- 339 Nicholas Sofroniew, Talley Lambert, Kira Evans, Juan Nuckolls, Peter Selber, and Orit Ziv. napari:  
340 a multi-dimensional image viewer for Python. *Zenodo*, 2022. doi: 10.5281/zenodo.3555620.
- 341 Salman F Banani, Hyun O Lee, Anthony A Hyman, and Michael K Rosen. Biomolecular condensates:  
342 organizers of cellular biochemistry. *Nature Reviews Molecular Cell Biology*, 18(5):285–298, 2017.  
343 doi: 10.1038/nrm.2017.7.
- 344 Jared A M Bard and D Allan Drummond. Chaperone regulation of biomolecular condensates.  
345 *Frontiers in Biophysics*, 2:1342506, 2024. doi: 10.3389/frbis.2024.1342506.

- 346 Lucas V Cairo, Xiaoyu Hong, Martin B D Müller, Patricia Yuste-Checa, Chandhuru Jagadeesan,  
347 Andreas Bracher, Sae-Hun Park, Manajit Hayer-Hartl, and F Ulrich Hartl. Stress-dependent  
348 condensate formation regulated by the ubiquitin-related modifier Urm1. *Cell*, 187(17):4656–  
349 4673.e28, 2024. doi: 10.1016/j.cell.2024.06.009.
- 350 Daniel S W Protter and Roy Parker. Principles and properties of stress granules. *Trends in Cell  
351 Biology*, 26(9):668–679, 2016. doi: 10.1016/j.tcb.2016.05.004.
- 352 Hendrik Glauninger, Jared A M Bard, Caitlin J Wong Hickernell, Karen M Velez, Edo M Airoldi,  
353 Weihan Li, Robert H Singer, Sneha Paul, Jingyi Fei, Tobin R Sosnick, Edward W J Wallace, and  
354 D Allan Drummond. Transcriptome-wide mRNP condensation precedes stress granule formation  
355 and excludes new mRNAs. *Molecular Cell*, 85(23):4393–4409.e11, 2025. doi: 10.1016/j.molcel.2025.  
356 11.003.
- 357 Peiguo Yang, Celine Mathieu, Regina-Maria Kolaitis, Peizhou Zhang, James Messing, Ugur Yurt-  
358 sever, Zhiming Yang, Jinjun Wu, Yuxin Li, Qingfei Pan, Jiou Yu, Eric W Martin, Tanja Mittag,  
359 Hong Joo Kim, and J Paul Taylor. G3bp1 is a tunable switch that triggers phase separation to  
360 assemble stress granules. *Cell*, 181(2):325–345.e28, 2020. doi: 10.1016/j.cell.2020.03.046.
- 361 Jordina Guillén-Boixet, Andrii Kopach, Alex S Holehouse, Sina Wittmann, Marcus Jahnel, Raimund  
362 Schlüßler, Kyoohyun Kim, Irmela R E A Trussina, Jie Wang, Daniel Mateju, Ina Poser, Shovamayee  
363 Maharana, Martina Rber-Sick, Odília Beutel, Arnaud Hubstenberger, Pascale Chazal, Kathrin  
364 Richter, Thomas Daiber, Anne Zondervan, Thomas Lengauer, Simon Alberti, and Anthony A  
365 Hyman. RNA-induced conformational switching and clustering of G3BP drive stress granule  
366 assembly by condensation. *Cell*, 181(2):346–361.e17, 2020. doi: 10.1016/j.cell.2020.03.049.
- 367 Jarrett Smith and David P Bartel. The G3BP stress-granule proteins reinforce the integrated stress  
368 response translation programme. *Nature Cell Biology*, 28(1):135–148, 2026. doi: 10.1038/s41556-  
369 025-01834-3.
- 370 David Pincus. Regulation of Hsf1 and the heat shock response. *Advances in Experimental Medicine  
371 and Biology*, 1243:41–50, 2020. doi: 10.1007/978-3-030-40204-4\_3.
- 372 Annisa Dea and David Pincus. The heat shock response as a condensate cascade. *Journal of Molecular  
373 Biology*, 436(14):168642, 2024. doi: 10.1016/j.jmb.2024.168642.
- 374 David Pincus. The unfolded protein response in fission yeast. *Journal of Molecular Biology*, 436(14):  
375 168640, 2024. doi: 10.1016/j.jmb.2024.168640.
- 376 David Shore, Sevil Zencir, and Benjamin Albert. Transcriptional control of ribosome biogenesis in  
377 yeast: links to growth and stress signals. *Biochemical Society Transactions*, 49(4):1589–1599, 2021.  
378 doi: 10.1042/BST20201136.
- 379 Séverine Boulon, Berndt J Westman, Saskia Hutten, François-Michel Boisvert, and Angus I Lamond.  
380 The nucleolus under stress. *Molecular Cell*, 40(2):216–227, 2010. doi: 10.1016/j.molcel.2010.09.024.

- 381 Denis L J Lafontaine, Joshua A Riback, Rümeysa Bascetin, and Clifford P Brangwynne. The  
382 nucleolus as a multiphase liquid condensate. *Nature Reviews Molecular Cell Biology*, 22(3):165–182,  
383 2021. doi: 10.1038/s41580-020-0272-6.
- 384 Emiliano Matos-Perdomo and Félix Machín. Nucleolar and ribosomal DNA structure under stress:  
385 yeast lessons for aging and cancer. *Cells*, 8(8):779, 2019. doi: 10.3390/cells8080779.
- 386 Carine Dominique, Nana Kadidia Maiga, Alfonso Méndez-Godoy, Benjamin Pillet, Hussein Hamze,  
387 Isabelle Léger-Silvestre, Yves Henry, Virginie Marchand, Valdir Gomes Neto, Christophe Dez,  
388 Yuri Motorin, Dieter Kressler, Olivier Gadal, Anthony K Henras, and Benjamin Albert. The  
389 dual life of disordered lysine-rich domains of snoRNPs in rRNA modification and nucleolar  
390 compaction. *Nature Communications*, 15(1):9415, 2024. doi: 10.1038/s41467-024-53805-1.
- 391 Asif Ali, Rania Garde, Olivia C Schaffer, Jared A M Bard, Kabir Husain, Sammy K Kik, Kimberly A  
392 Davis, Sofia Luengo-Woods, Maya G Igarashi, D Allan Drummond, Dilip Bhatt, Anshul S Bhatt,  
393 and David Pincus. Adaptive preservation of orphan ribosomal proteins in chaperone-dispersed  
394 condensates. *Nature Cell Biology*, 25(11):1691–1703, 2023. doi: 10.1038/s41556-023-01253-2.
- 395 Asif Ali, Sarah Paracha, and David Pincus. Preserve or destroy: Orphan protein proteostasis and the  
396 heat shock response. *Journal of Cell Biology*, 223(12):e202407123, 2024. doi: 10.1083/jcb.202407123.
- 397 Harsha Garadi Suresh, Eric Bonneil, Benjamin Albert, Carine Dominique, Michael Costanzo,  
398 Carles Pons, Myra Paz David Masinas, Ermira Shuteriqi, David Shore, Anthony K Henras,  
399 Pierre Thibault, Charles Boone, and Brenda J Andrews. K29-linked free polyubiquitin chains  
400 affect ribosome biogenesis and direct ribosomal proteins to the intranuclear quality control  
401 compartment. *Molecular Cell*, 84(12):2337–2352.e9, 2024. doi: 10.1016/j.molcel.2024.05.018.
- 402 Daniel Kaganovich, Ron Kopito, and Judith Frydman. Misfolded proteins partition between  
403 two distinct quality control compartments. *Nature*, 454(7208):1088–1095, 2008. doi: 10.1038/  
404 nature07195.
- 405 Emily Mitchell Sontag, Rahul S Samant, and Judith Frydman. Mechanisms and functions of spatial  
406 protein quality control. *Annual Review of Biochemistry*, 86:97–122, 2017. doi: 10.1146/annurev-  
407 biochem-060815-014616.
- 408 Emily M Sontag, Fabián Morales-Polanco, Jian-Hua Chen, Gerry McDermott, Patrick T Dolan,  
409 Daniel Gestaut, Mark A Le Gros, Carolyn Larabell, and Judith Frydman. Nuclear and cytoplasmic  
410 spatial protein quality control is coordinated by nuclear-vacuolar junctions and perinuclear  
411 ESCRT. *Nature Cell Biology*, 25(5):699–713, 2023. doi: 10.1038/s41556-023-01128-6.
- 412 Nancy Kedersha, Marc D Panas, Christopher A Achorn, Shawn Lyons, Sarah Tisdale, Tyler Hick-  
413 man, Marshall Thomas, Judy Lieberman, Gerald M McInerney, Pavel Ivanov, and Paul Anderson.  
414 G3BP–Caprin1–USP10 complexes mediate stress granule condensation and associate with 40S  
415 subunits. *Journal of Cell Biology*, 212(7):845–860, 2016. doi: 10.1083/jcb.201508028.

- <sup>416</sup> Samuel J Lord, Katlyn B Velle, R Dyche Mullins, and Lillian K Fritz-Laylin. SuperPlots: Communi-  
<sup>417</sup> cating reproducibility and variability in cell biology. *Journal of Cell Biology*, 219(6):e202001064,  
<sup>418</sup> 2020. doi: 10.1083/jcb.202001064.
- <sup>419</sup> Sylvain V Costes, Dirk Daelemans, Eul Hyun Cho, Zachary Dobbin, George N Pavlakis, and  
<sup>420</sup> Stephen J Lockett. Automatic and quantitative measurement of protein-protein colocalization in  
<sup>421</sup> live cells. *Biophysical Journal*, 86(6):3993–4003, 2004. doi: 10.1529/biophysj.103.038422.
- <sup>422</sup> Stanley E Lazić. What exactly is ‘N’ in cell culture and animal experiments? *PLoS Biology*, 16(4):  
<sup>423</sup> e2005282, 2018. doi: 10.1371/journal.pbio.2005282.
- <sup>424</sup> Rania Garde, Annisa Dea, Madeline F Herwig, Asif Ali, and David Pincus. Feedback control of  
<sup>425</sup> the heat shock response by spatiotemporal regulation of Hsp70. *Journal of Cell Biology*, 223(12):  
<sup>426</sup> e202401082, 2024. doi: 10.1083/jcb.202401082.

427 **Supplemental Materials**

428 **Supplemental Figure 1.** Complete set of QC overlays for mammalian cell dataset.

429 **Supplemental Figure 2.** Complete set of QC overlays for yeast temperature series.

430 **Supplemental Figure 3.** All 21 superplot metrics from yeast temperature series analysis.

431 **Supplemental Table 1.** Complete parameter settings for mammalian and yeast analyses (from  
432 config\_used.yml).

433 **Supplemental Table 2.** Per-cell quantification data (cells.csv) for both datasets.

434 **Supplemental Table 3.** Pairwise colocalization metrics for yeast temperature series.

435 **Supplemental Table 4.** Nucleolar proximity measurements for yeast temperature series.

436 **Supplemental Table 5.** Nucleolar morphology measurements for yeast temperature series.